Available online at www.sciencedirect.com
SCIENCE DIRECT
Remote Sensing of Environment 99 (2005) 2 – 15
Remote Sensing of Environment
www.elsevier.com/locate/rse

Characterizing partial upwellings and surface circulation at Lake Tahoe, California–Nevada, USA with thermal infrared images

Todd E. Steissberg [a,*], Simon J. Hook [b], S. Geoffrey Schladow [a,c]

[a] Department of Civil and Environmental Engineering, University of California, Davis, USA
[b] Jet Propulsion Laboratory, California Institute of Technology, Pasadena, California, USA
[c] Tahoe Environmental Research Center, University of California, Davis, CA 95616, USA

Received 16 September 2004; received in revised form 27 May 2005; accepted 20 June 2005

Abstract

Thermal infrared data from recently launched satellite instruments provide an opportunity to address key scientific questions and develop new applications, which could not be addressed or developed with data from earlier instruments. The satellite instruments that provide these data include ASTER, Landsat ETM+, and MODIS, and this study demonstrates how data from them can be used to map upwelling and circulation associated with the transport of heat, solutes, and particles in lakes. Upwelling in a density-stratified water body such as a lake or reservoir results from a surface wind stress being balanced by a horizontal pressure gradient, causing denser water to rise at the upwind lake boundary. Upwellings are considered partial when intermediate-depth water reaches the surface and total when bottom water surfaces. Upwellings are an important part of ecosystem functioning, since they transport nutrients from deeper in the lake, where they accumulate, to the surface layer, where they facilitate phytoplankton growth. Thermal infrared images acquired by ASTER, ETM+, and MODIS can be used to observe partial upwelling events in lakes and provide insight into their spatial variability and horizontal distribution, information totally lacking from conventional in situ measurements. At Lake Tahoe, partial upwellings were found to occur every few days throughout the spring and summer, transporting water from 10–30 m below the surface to the surface layer. They commonly display a jet-like appearance, traveling from the upwind to the downwind side of the lake, with current speeds of 12–17 cm/s. Partial upwellings were found to generally decrease lake clarity, although deeper upwelling events can increase clarity. Sinking zones, other convergence areas, and divergence areas were also observed. The temperature variability associated with upwelling, which could be clearly mapped in the thermal infrared satellite images, illustrates the advantage of synoptic thermal infrared satellite measurements over in situ point measurements alone for detecting upwelling events, since, depending on location, an in situ instrument might not capture an upwelling event. The spatial information conveyed by the synoptic satellite measurements can be used to help improve monitoring of the clarity and general water quality of Lake Tahoe.

Keywords: Partial upwelling; Surface currents; Circulation; Thermal infrared; ASTER; MODIS; Landsat ETM+; Clarity; Water quality; Lake Tahoe

1. Introduction

Since the launch in 1972 of the first ERTS satellite, later renamed Landsat, high spatial resolution data acquired by satellite instruments have been used for studies of inland water processes (Rogers et al., 1976). The majority of these studies have focused on the use of data from the visible wavelengths (0.4–0.7 μm) rather than the thermal infrared wavelengths (8–12 μm). Visible data can be used to look at changes in the clarity and color of the water associated with changes in sediment input or the amount of chlorophyll (Choubey, 1998). Thermal infrared data can be used to look at changes in the surface temperature associated with upwellings or changes in circulation (Ikeda & Emery, 1984; Schladow et al., 2004). There are several reasons why the majority of studies to date have focused on the use

* Corresponding author.
E-mail address: tsteissberg@ucdavis.edu (T.E. Steissberg).

0034-4257/$ - see front matter © 2005 Elsevier Inc. All rights reserved.
doi:10.1016/j.rse.2005.06.011

of visible rather than thermal infrared data. These include the typically higher spatial resolution, greater number of spectral bands, and higher signal-to-noise ratio of the visible data.

Recently, several satellite instruments that utilize new technology to overcome these limitations have been launched. For example, the early Landsats included the Thematic Mapper (TM) instrument, which had a single thermal band (10–11 μm) with a spatial resolution of 120 m and NEΔT (noise-equivalent temperature difference) of ≤0.30 at 280 K (Barsi et al., 2003). In 1999, a next-generation Landsat was launched, which included the Enhanced Thematic Mapper Plus (ETM+). ETM+ also has a single thermal band (10.31–12.36 μm), but with an improved spatial resolution of 60 m and improved NEΔT of 0.22 at 280 K (Barsi et al., 2003). The launch of Landsat ETM+ was followed by the launch of the first Earth Observing System (EOS) platform, subsequently named Terra, which included the Advanced Spaceborne Thermal Emission and Reflection Radiometer (ASTER) and Moderate Resolution Imaging Spectroradiometer (MODIS). ASTER includes five spectral bands in the thermal infrared (Table 2), each with a spatial resolution of 90 m and NEΔT of ≤0.3 K (Yamaguchi et al., 1998). MODIS has three bands in the thermal infrared designed to measure surface temperature with a spatial resolution of 1 km and detector NEΔT's of 0.020 K (Band 29; 8.4–8.7 μm), 0.024 K (Band 31; 10.78–11.28 μm) and 0.040 K (Band 32; 11.77–12.27 μm) at 300 K (Barnes et al., 1998). Landsat and ASTER thermal infrared data can typically be acquired twice every 16 days (a day and a night acquisition) at a given location, although Landsat does not record data at night, unless by special request. MODIS data can typically be acquired daily due to the larger scan angle of MODIS. These new instruments provide an opportunity to develop new applications with thermal infrared data in order to address key scientific questions that could not be addressed with the earlier instruments.

1.1. Wind-driven upwelling

Lakes generally stratify from the late spring to early fall when increased solar radiation combined with wind-forced and convective mixing form a warm layer of lower-density water at the surface. The lake then becomes divided into three layers, the epilimnion (warm surface layer), the hypolimnion (cool bottom layer), and the metalimnion (intermediate-density transition zone between the epilimnion and hypolimnion). Typical temperature-profile data from the stratified period, collected at the LTP (Lake Tahoe Productivity) station (Fig. 1) from June 17–August 26, 2002, are shown in Fig. 2, with these layers delineated. Photosynthesis generally occurs throughout the epilimnion and upper metalimnion (euphotic zone), while detrital material and associated nutrients sink, accumulating in the metalimnion and hypolimnion, where they cannot be

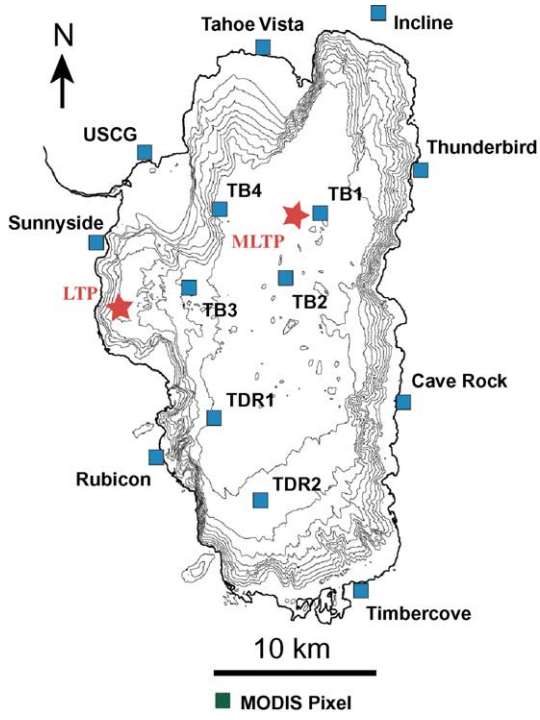

Fig. 1. Lake Tahoe, showing buoys, rafts, land stations, sampling locations, 50-m contours, and MODIS pixel size relative to Lake Tahoe.

utilized by phytoplankton. Lake ecosystem functioning is therefore dependent on processes that re-entrain nutrients into the sunlit euphotic zone. Field data from lakes indicate that the vertical fluxes of heat, solutes, and particles are largely determined by processes occurring at lake boundaries (MacIntyre et al., 1999; MacIntyre & Jellison, 2001). Materials, both particulate and dissolved, are transported away from the boundaries by horizontal motions. One process that accomplishes both vertical transport at the boundary and horizontal transport away from the boundary is wind-driven upwelling. Upwelling in a density-stratified water body, such as a lake or reservoir, results from a surface wind stress being balanced by a horizontal pressure gradient, causing denser water to rise at the upwind lake boundary (Monismith, 1985, 1986; Stevens & Imberger, 1996; Farrow & Stevens, 2003). Upwellings are considered partial when intermediate-depth (metalimnetic) water reaches the surface and total when bottom (hypolimnetic) water surfaces (Monismith, 1986). They are an important part of ecosystem functioning, since they transport nutrients to the surface layer (MacIntyre, 1993, 1998; MacIntyre & Jellison, 2001), which facilitates phytoplankton growth.

Upwellings of water into the surface layer, the subsequent transport of the water and associated materials away from a lake boundary by surface currents, and the eventual gravitational return of these dense waters to depth are not fully understood. Since full and partial wind-driven upwelling also occur at coastal margins, upwelling and associated boundary mixing have direct bearing on a range of

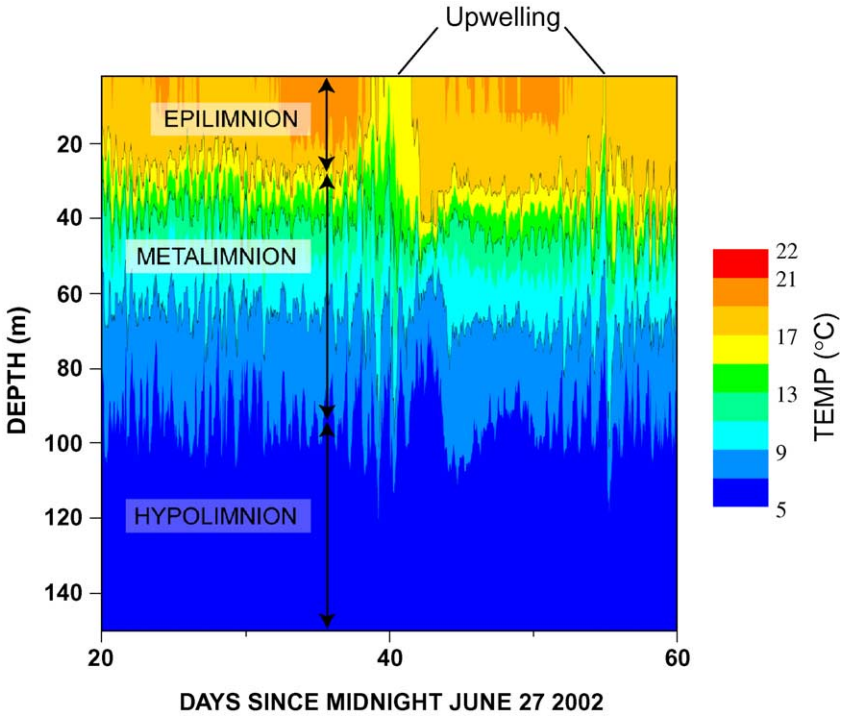

Fig. 2. Temperature contours from thermistor-chain data measured at the LTP station, June 17–August 26, 2002. Two partial upwellings are indicated on August 6–8 and August 20, 2002. Location of LTP station shown in Fig. 1.

important issues, including the fate of nutrients and contaminants introduced into inland and coastal waters (Howarth, 1993), larval dispersion in the coastal zone (Wing et al., 1995), and fish production (Ostrovsky et al., 1996; Mann, 2000). The present study compares high-resolution thermal infrared satellite data from ASTER and ETM+ and moderate-resolution data from MODIS, and reports on how these data can be used to map upwelling and circulation in lakes.

1.2. Site description

Lake Tahoe (Fig. 1) is a large lake situated in a granite graben near the crest of the Sierra Nevada Mountains on the California–Nevada border, at 39° N, 120° W. The lake level is approximately 1895 m above mean sea level. The lake is roughly oval in shape with a N–S major axis (33 km long, 18 km wide), and has a surface area of 500 km^2. The land portion of the watershed has an area of 800 km^2. Lake Tahoe is the 11th deepest lake in the world, with an average depth of 330 m and a maximum depth of 501 m. Due to its large volume and proportionately small watershed, Lake Tahoe is a highly oligotrophic (clear, low-productivity) lake. As with most lakes, the surface layer (epilimnion) of Lake Tahoe deepens during the fall and winter; however, complete vertical mixing only occurs every few years (Jassby et al., 1999). Due to its large thermal mass, Lake Tahoe does not freeze in the winter. Lake Tahoe is an ideal natural laboratory; its size and depth make it a good analog for coastal as well as lake systems, and its many cloud-free days and high altitude make it ideal for acquiring remotely sensed data (Hook et al., 2003). A large body of research exists for Lake Tahoe, primarily due to concern over its diminishing clarity (Jassby et al., 1999), a consequence of both increased phytoplankton production and particulate concentrations.

The Lake Tahoe automated validation site was established in 1999 to help validate the thermal infrared data and products from the ASTER and MODIS instruments on the Terra spacecraft, launched December 18, 1999 (Salomonson et al., 1989; Yamaguchi et al., 1998). Work at the site is performed by the Jet Propulsion Laboratory and the University of California, Davis. A detailed description of the site is given in Hook et al. (2003) and summarized here for completeness. Measurements at the site are made from four permanently moored buoys on the lake, subsequently referred to as TB1, TB2, TB3, and TB4, and several stations on the shore of the lake (Fig. 1). Each buoy has a custom-built radiometer that measures the skin (top 10–1000 μm) temperature and several temperature sensors that measure the bulk kinetic water temperature at a depth of 2 cm. During the monitoring period, meteorological stations were added to each buoy. The meteorological measurements include wind speed, wind direction, relative humidity, air temperature, atmospheric pressure, and net radiation. A full set of measurements (meteorology, bulk and skin temperatures) is made every 2 min and stored on data loggers, which are downloaded either daily via phone modem or

every few months during site visits. In addition, hourly averaged wind speed and direction measurements are recorded at the Thunderbird Lodge (TBLG) site maintained by the Tahoe Regional Planning Agency (TRPA; www.trpa.org) (Fig. 1).

During the study period, each buoy had a single custom-built self-calibrating Mk I radiometer (2000) or Mk II radiometer (2001–present) for measuring the skin temperature. The Mk I had an accuracy of ±0.2 °C, and the Mk II radiometer has an accuracy of ±0.1 °C. The radiometer is mounted on a pole that extends beyond the buoy, approximately 1 m above the water surface. The sensor used in the radiometer is a thermopile detector with a germanium lens embedded in a copper thermal reservoir. The sensor passes radiation with wavelengths between 7.8 and 13.6 μm. In order to obtain the skin (kinetic) temperature, it is necessary to correct the data for any atmospheric and emissivity effects (Hook et al., 2003). The skin temperature is derived by correcting for surface emissivity, subtracting the sky radiance reflected by the surface into the path of the radiometer, and converted to skin temperature using Planck's equation (emissivity = 1.0). The emissivity of water was obtained from the ASTER spectral library (http://speclib.jpl.nasa.gov). Further details are provided in Hook et al. (2003).

Four different types of bulk temperature sensors have been deployed at Lake Tahoe. These are the "Optic Stowaway" (8-bit data), "Hobo Water Temp Pro," "Hobo Pro Temp/External Temp," and "MBLTA" sensors (all 12-bit data). The four types of sensors have manufacturer-specified accuracies of ±0.25 °C, ±0.20 °C, ±0.20 °C, ±0.10 °C, respectively. After recalibration, the 12-bit sensors are accurate to ±0.1 °C. The MBLTA sensors are semiconductors and are manufactured by Apprise Technologies. All the other sensors are thermistors and are manufactured by the Onset Computer Corporation.

Both NASA/JPL and UC Davis maintain additional equipment at the US Coast Guard Station. This includes a full meteorological station (wind speed, wind direction, relative humidity, air temperature and atmospheric pressure), a full radiation station (longwave and shortwave radiation, up and down), a shadow-band radiometer, and an all-sky camera. UC Davis also maintains two additional rafts in the southern part of Lake Tahoe (Fig. 1); these measure meteorological variables and bulk water temperature. The locations of the buoys are given in Table 1. TB2 and TB3 were moved slightly farther south during the monitoring period. In addition, routine monitoring of water quality in the lake is conducted by the Tahoe Environmental Research Center (TERC) every 1–2 weeks. This monitoring includes Secchi depth measurements, defined as the depth at which a 20-cm white disk is no longer visible from the surface. Lake Tahoe's Secchi depth measurements have consistently used a 20-cm white disk. Secchi depths are a standard measure of water clarity. Lake Tahoe's annual average Secchi depth is currently 22 m, a reduction of almost 10 m in the last 30 years. Nutrient and chlorophyll concentrations are also measured at fixed depths. Nutrients typically increase with depth, as they are depleted by phytoplankton growth in the upper part of the water column. Lake Tahoe is characterized by low chlorophyll concentrations, similar to the open ocean. The maximum chlorophyll concentrations occur at a depth of 60–80 m and are typically 2–4 μg L^{-1}, whereas surface concentrations are generally below 1 μg L^{-1}. Thus partial upwelling events should be expected to generally increase surface chlorophyll concentrations and decrease clarity (chlorophyll and associated particulate matter attenuate visible light). However, a particularly deep partial upwelling could conceivably bring high-clarity, low-chlorophyll water to the surface, in similar fashion to a full upwelling (Schladow et al., 2004).

Table 1
NASA buoy locations on Lake Tahoe

Buoy	7 May 1999–31 Oct 2002	31 Oct 2002–2 Nov 2002	2 Nov 2002–Present
TB1	39° 09.180 N 120° 00.020 W	39° 09.180 N 120° 00.020 W	39° 09.180 N 120° 00.020 W
TB2	39° 08.292 N 120° 00.018 W	39° 08.292 N 120° 00.018 W	39° 06.562 N 120° 00.645 W
TB3	39° 08.300 N 120° 04.920 W	39° 06.612 N 120° 04.521 W	39° 06.612 N 120° 04.521 W
TB4	39° 09.300 N 120° 04.330 W	39° 09.300 N 120° 04.330 W	39° 09.300 N 120° 04.330 W

The thermal stratification in Lake Tahoe is moderate, and is spread over a broad metalimnion. Fig. 2 shows typical summer temperature contours from July 17–August 26, 2002, measured at the LTP station (Fig. 1). The metalimnion extends from 20–70 m, with temperatures ranging from 9–17 °C. The oscillations in the temperature contours are the result of the complex internal-wave field present at Lake Tahoe. Full upwellings occur rarely in Lake Tahoe, and these have only been observed in the winter or late fall. During the spring and summer stratified period, the broad metalimnion and moderate stratification, combined with the lake's great depth, make Lake Tahoe particularly susceptible to large-amplitude internal waves (Rueda et al., 2003) associated with partial upwelling. A partial upwelling event is visible from August 6–8, 2002, during which 15 °C water is transported to the surface. A second smaller partial upwelling event occurred on August 22nd. Full upwellings occur rarely in Lake Tahoe due to its deep thermocline and great overall depth (Abbott et al., 1984; Schladow et al., 2004), whereas partial upwellings, which are the focus of this research, occur frequently.

1.3. Data sources

A variety of data sources were used to study the partial upwellings and circulation in Lake Tahoe. These included thermal infrared data from ASTER, ETM+, and MODIS,

Table 2
Thermal infrared instrument characteristics for ASTER, ETM+, MODIS, and AVHRR

Instrument	Satellite	Band	Bandwidth (μm)	Spatial resolution (m)	NEΔT (K)
ASTER[a]	Terra	10	8.125 – 8.475	90	≤0.3 @ 280K
		11	8.475 – 8.825		
		12	8.925 – 9.275		
		13	10.25 – 10.95		
		14	10.95 – 11.65		
ETM+[b]	Landsat-7	6	10.31 – 12.36	60	0.22 @ 300 K
MODIS[c]	Terra	29	8.400 – 8.700	1000	0.020 @ 300 K
		31	10.780 – 11.280		0.024 @ 300 K
		32	11.770 – 12.270		0.040 @ 300 K
AVHRR[d]	NOAA-6, 7–12, 14	4	10.30 – 11.30	1100	0.12 @ 300 K
	NOAA-7, 9, 11, 12, 14	5	11.50 – 12.50		0.12 @ 300 K

[a] Yamaguchi et al. (1998).
[b] Barsi et al. (2003).
[c] Barnes et al. (1998).
[d] EOSDIS, http://eosims.cr.usgs.gov:5725/sensor_documents/avhrr_sensor.html.

as well as in situ water temperature and meteorological measurements. Only the thermal infrared data from the three satellite instruments were used in this study. The instrument specifications related to the thermal infrared channels from each instrument are summarized in Table 2. ASTER and MODIS (both on Terra) have nominal equator crossings around 10:30 AM/PM, while ETM+ (onboard Landsat) has an equator crossing time around 10:00 AM/PM local time. Terra and Landsat are in similar polar orbits, with Terra following ~30 min behind Landsat.

These data sources improve considerably on the field data and the AVHRR thermal infrared satellite data used in earlier studies (Strub et al., 1984; Strub & Powell, 1986, 1987) to study large-scale surface current velocity and circulation at Lake Tahoe. Detailed descriptions of ASTER, MODIS, and Landsat ETM+ can be found in Yamaguchi et al. (1998), Salomonson et al. (1989), and Barsi et al. (2003), respectively.

2. Data processing

2.1. Satellite data

ASTER, ETM+, and MODIS data are provided as at-sensor radiance. The surface temperature and emissivity derived from the at-sensor radiance are also available for ASTER and MODIS. This study utilized the at-sensor radiance data corrected by the authors to surface (skin) temperature. The standard surface temperature and emissivity data products available for ASTER and MODIS were not used because the algorithms used to generate them left residual artifacts, which were undesirable for this study. The at-sensor radiance (Ls) for a given wavelength (λ) in the thermal infrared can be written as:

$$Ls_\lambda = \left[\varepsilon_\lambda L_{bb\lambda}(T) + (1-\varepsilon_\lambda)\pi^{-1}E_{sky\lambda}\right]\tau_\lambda + L_{atm\lambda} \quad (1)$$

where:

ε_λ surface emissivity at wavelength λ.
$L_{bb\lambda}(T)$ spectral radiance from a blackbody at surface temperature T.
$E_{sky\lambda}$ downwelling sky irradiance incident upon the surface from the atmosphere.
τ_λ transmittance (spectral atmospheric transmission).
$L_{atm\lambda}$ path radiance (spectral upwelling radiance from atmospheric emission and scattering that reaches the sensor).

The effect of τ_λ is to reduce the amount of ground emitted radiance measured at the sensor. $L_{atm\lambda}$ adds a component unrelated to the ground, and $E_{sky\lambda}$ serves to reduce the spectral contrast since the deeper an emissivity feature, the more it is "filled in" by reflected downwelling radiation due to Kirchhoff's Law. Any algorithm that produces a fundamental geophysical parameter (surface radiance, temperature, or emissivity), must compensate for these atmospheric effects.

Table 3
Mean differences ($\Delta T = T_{image} - T_{buoy}$) and standard deviations of derived (satellite) and measured (buoy radiometer) skin temperatures

Instrument	Image Date	Image Time (UTC)	Mean ΔT (°C)	Std. Dev. ΔT (°C)
ETM+	Jun 03, 2001	18:28	−0.08	0.18
ASTER	Jun 03, 2001	19:06	−0.04	0.05
MODIS	Jun 03, 2001	19:06	−0.07	0.22
MODIS	Jun 04, 2001	6:10	0.22	0.01
ETM+	Jul 21, 2001	18:28	0.19	0.36
ASTER	Jul 22, 2001	6:09	0.06	0.09
MODIS	Jul 21, 2001	19:05	0.08	0.34
MODIS	Jul 22, 2001	6:09	−0.01	0.10
ASTER	Jun 06, 2002	18:58	−0.04	0.59
ASTER	Jun 07, 2002	6:02	0.14	0.11
MODIS	Jun 06, 2002	18:58	−0.52	0.67
MODIS	Jun 07, 2002	6:03	−0.13	0.12

Once the atmospheric effects have been removed, the surface radiance is given by:

$$L_\lambda = \varepsilon_\lambda L_{BB\lambda}(T) \quad (2)$$

or

$$L_{BB\lambda} = \frac{C_1}{\lambda^5 \pi \left[e\left(\frac{C_2}{\lambda T} \right) - 1 \right]} \quad (3)$$

where:

L_λ = emitted radiance
$L_{BB\lambda}$ = blackbody radiance ($Wm^{-2}\ \mu m^{-1}\ sr^{-1}$)
λ = wavelength of channel (m)
T = temperature of blackbody (Kelvin)
C_1 = first radiation constant = 3.7415×10^{-16} (Wm^2)
C_2 = second radiation constant = 0.0143879 (m deg)
$\varepsilon\lambda$ = surface emissivity (0–1).

The path transmittance, path radiance, and downwelling irradiance terms were obtained from a radiative transfer model (MODTRAN 3.5). Atmospheric profiles obtained from the National Centers for Environmental Prediction (NCEP), interpolated to the overpass time, were used as

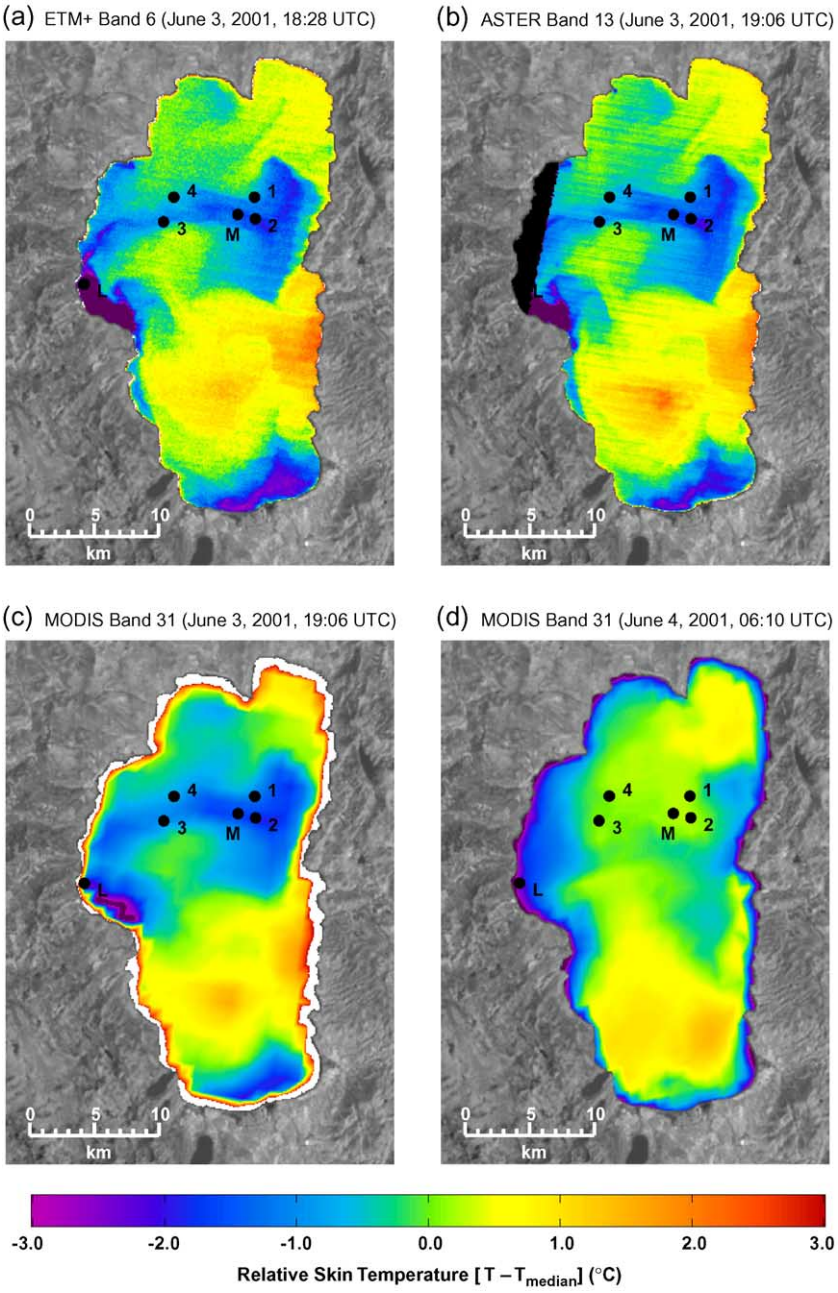

Fig. 3. Satellite images acquired June 3–4, 2001, showing relative skin temperatures. The median skin temperatures are: (a) 12.8 °C (b) 12.9 °C (c) 13.1 °C (d) 11.8 °C The Landsat ETM+ image and MODIS images were resampled to regular 90-m grids using bilinear interpolation. Stations: L = LTP, M = MLTP, 1–4 = TB1–TB4.

inputs to the model. NCEP produces global model values on a $1° \times 1°$ grid at 6-h intervals. Lake Tahoe is centered on 39°N, 120°W, and the grid value for this point was utilized. The radiative transfer model was run at full resolution (1 wave number) and the result convolved to the system response functions for the appropriate bands of ETM+, ASTER, and MODIS. The emissivity of water was obtained from the ASTER spectral library (http://speclib.jpl.nasa.gov). The at-sensor radiance data from ASTER, MODIS, and ETM+ were obtained from the EOS Data Active Archive Centers (DAAC's) accessible from http://edcimswww.cr.usgs.gov/pub/imswelcome/. ASTER Band 13, ETM+ Band 6 (high gain), and MODIS Band 31 were used, since these bands have the greatest atmospheric transmissivity.

In order to assess the method used to derive the skin temperature from the satellite data, the satellite-derived (image) skin temperatures were compared to the in situ (buoy) radiometer-derived skin temperatures. The image pixel temperature at each buoy was computed using bilinear interpolation. The average differences ($\Delta T = T_{\text{image}} - T_{\text{buoy}}$) and standard deviations of the satellite and in situ skin temperatures are shown in Table 3. The satellite-derived skin temperatures were in good agreement with the in situ skin temperatures for all images except for the MODIS

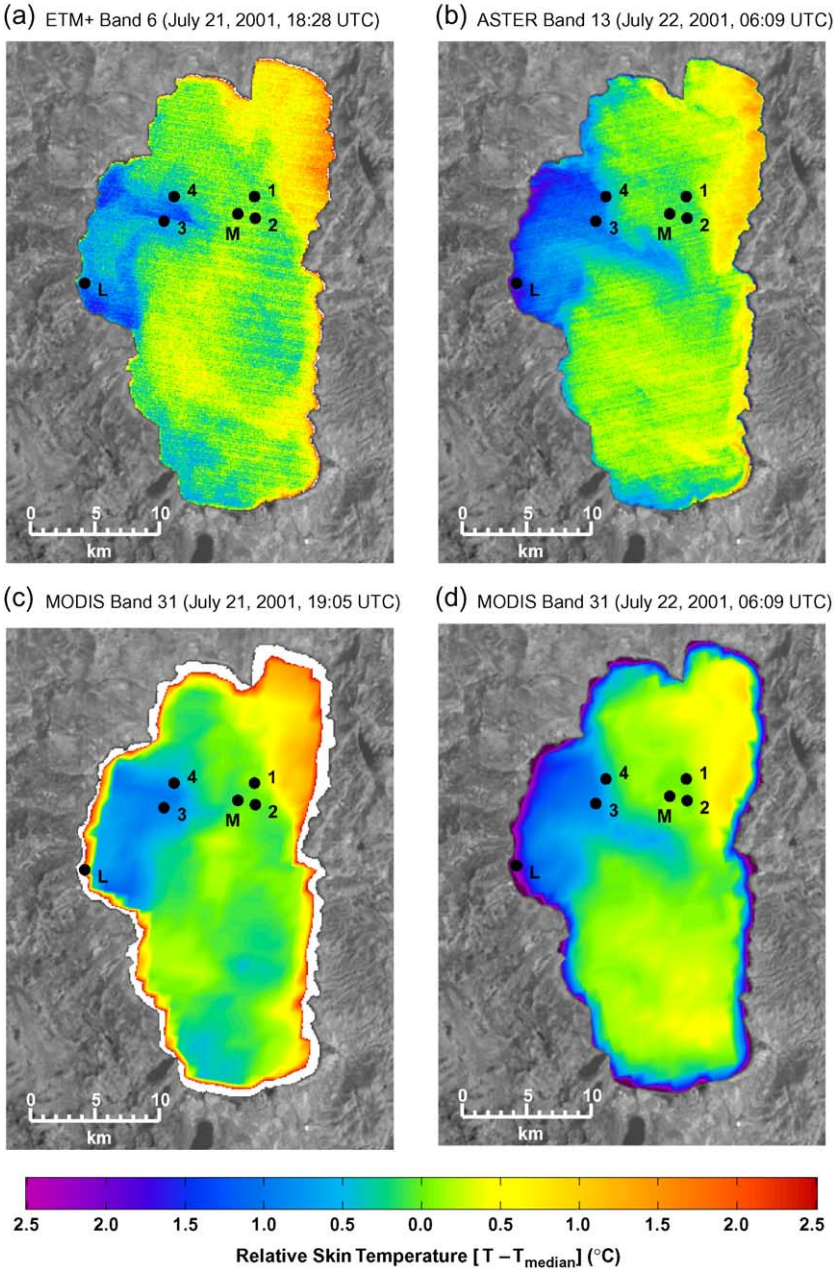

Fig. 4. Satellite images acquired July 21–22, 2001, showing relative skin temperatures. The median skin temperatures are: (a) 16.1 °C (b) 15.8 °C (c) 16.5 °C (d) 15.8 °C The Landsat ETM+ image and MODIS images were resampled to regular 90-m grids using bilinear interpolation. Stations: L = LTP, M = MLTP, 1–4 = TB1–TB4.

image acquired June 6, 2002 at 18:58 UTC. This could be partly due to contamination of the 1-km pixels by sub-visible cirrus. However, most of the difference is likely due to the variability in the temperature of the water surface, as indicated by the low mean ΔT but elevated standard deviation of the coincident ASTER image. The effects of the averaging in the MODIS pixels can be seen when visually comparing the ASTER and MODIS images at the buoys (Fig. 5).

In order to compare the skin temperature maps derived from the various satellite datasets, the 60-m ETM+ images and 1-km MODIS images were resampled to 90-m to match the ASTER spatial resolution, using bilinear interpolation. The resulting temperature maps (Figs. 3–5) are displayed as relative skin temperature, obtained by subtracting the median skin temperature of each image from all of the pixels in each image, to compensate for lakewide differences in temperature between successive images, due to diurnal heating or cooling. This allowed plotting all four images on the same relatively narrow temperature scale to clearly display the thermal patterns in all of the images. The color scales in Figs. 3–5 are centered on zero, so that the median temperature is displayed in green in each image. Temperatures below the minimum temperature in the color

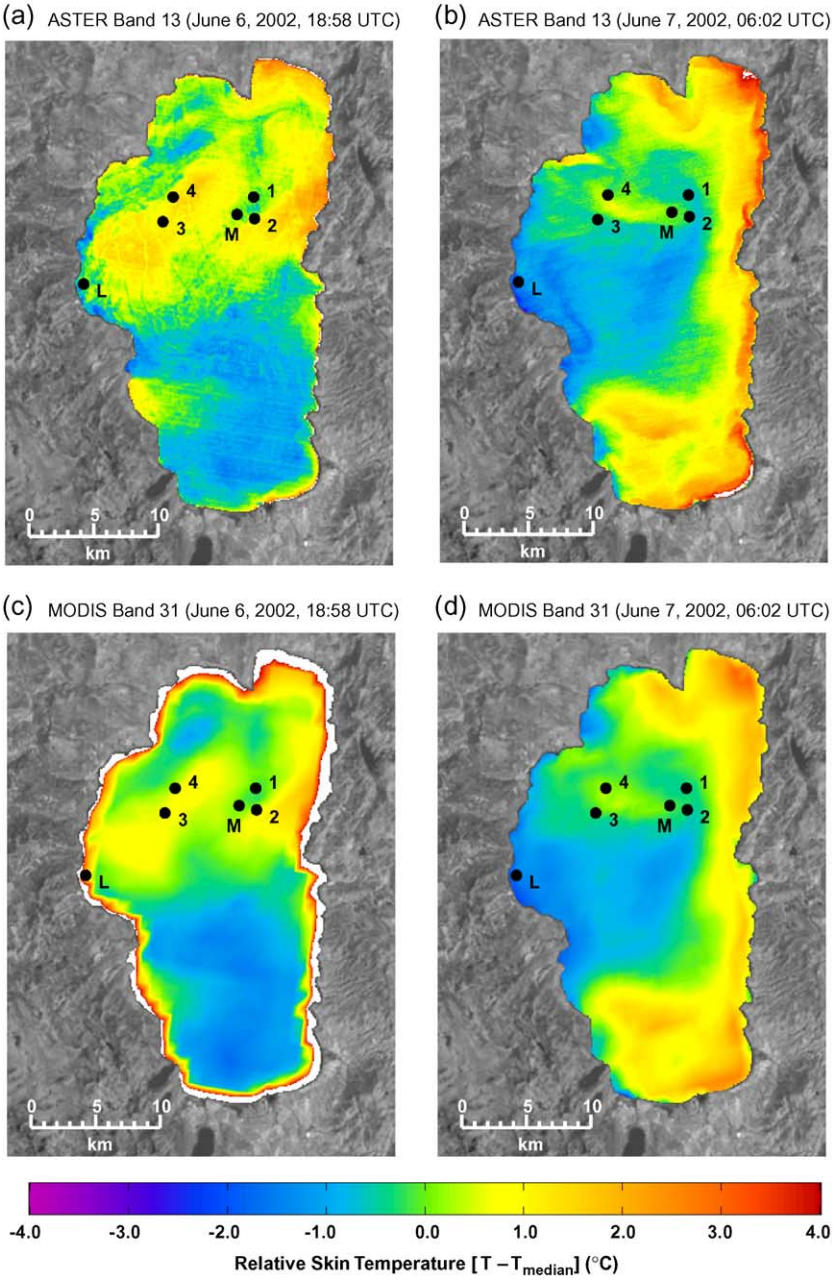

Fig. 5. (a) Satellite images acquired June 6–7, 2002, showing relative skin temperatures. The median skin temperatures are: 15.7 °C (b) 12.7 °C (c) 16.6 °C (d) 13.0 °C The MODIS images were resampled to a regular 90-m grid using bilinear interpolation. Stations: L = LTP, M = MLTP, 1–4 = TB1–TB4.

scale were masked in dark purple, while those above the maximum were masked in white. Missing pixels (Fig. 3b) were masked in black. In the MODIS images, the prominent white borders near the lake boundaries in the daytime images and purple borders near the lake boundaries in the nighttime images are the result of contamination of the pre-interpolated 1-km pixels by warmer (daytime) or cooler (nighttime) land pixels. The daytime temperature difference between the land and the water surface is larger than the nighttime difference, which accounts for the more-pronounced border in the daytime images. Any dates and times given for the satellite and in situ data are in UTC. The standard local time (Pacific Standard Time, PST) is UTC minus eight hours.

2.2. Field data

The bulk water temperature datasets were cleaned to remove data spikes and sections of data where sensors failed or drifted, as determined by cross-comparison among the various sensors. It should be emphasized that each buoy had a redundant system of several bulk-temperature sensors to improve quality assurance. The "cleaned" data for each temperature sensor were interpolated to a regular 2-min time grid. The interpolated data were then averaged for each set of sensors (MBLTA, Stowaway, Hobo) for each buoy. The mean bulk-water temperatures measured at each buoy by the Stowaway thermistors are displayed in Figs. 6–8. To facilitate upwelling detection, the 12-h running mean was subtracted from the buoy temperature data. Wind speed and direction were cross-compared among TB3, TB4, TDR1, TDR2, Sunnyside, USCG, and TBLG (Fig. 1). The hourly averaged wind speed and wind direction measured at TB3 are shown in Figs. 6–8. The red vertical lines in Figs. 6–8 indicate the times of acquisition of the MODIS images shown in Figs. 3–5c and d, respectively.

3. Discussion

Nine partial upwelling events (Table 4) detected by ASTER were analyzed for 2000–2002. Three of these events are shown in Figs. 3–5. Each nighttime ASTER overpass has either a corresponding daytime ASTER image or ETM+ image, acquired ~11 h earlier. These are subsequently referred to as day/night image pairs. For each daytime ASTER image, there typically exists a corresponding daytime ETM+ image acquired ~40 min earlier. These are subsequently referred to as day/day image pairs. Fig. 3 shows a day/day pair acquired June 3, 2001. Fig. 4 shows a day/night ASTER/ETM+ pair acquired July 21–22, 2001. Fig. 5 shows a day/night ASTER/ASTER pair acquired June 6–7, 2002. The 1-km MODIS data are nearly always available since MODIS is always on (day and night).

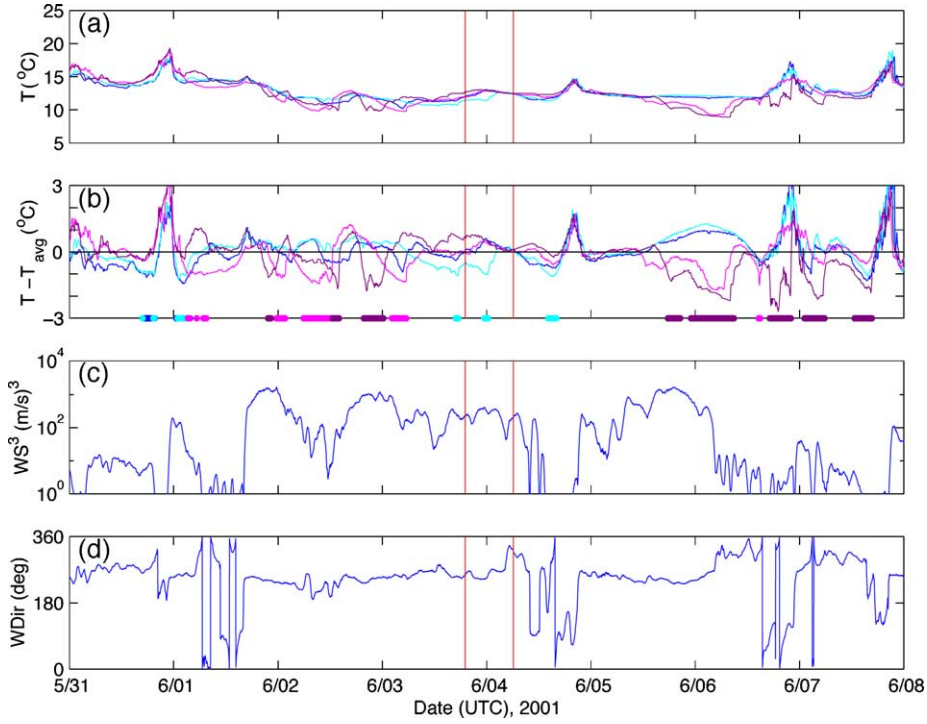

Fig. 6. Field data corresponding to the June 2001 images. (a) Average water temperature measured by the Stowaway thermistors at the NASA buoys. TB1 = blue, TB2 = cyan, TB3 = magenta, TB4 = purple. Blue shades denote the two eastern buoys, while purple shades denote the two western buoys. The darker shades denote the two northern buoys, while the lighter shades denote the two southern buoys. (b) Difference from the 12-h running mean of the average temperature for all buoys. Colored dots on the *x*-axis indicate points more than 1 °C cooler than the 12-h running mean temperature. (c) Wind speed cubed (analog of wind power) computed from wind speed measured at TB3. (d) Wind direction (WDir) measured at TB3, in degrees clockwise from True North. Red vertical lines denote the times of MODIS images. Buoy locations shown in Fig. 3, and latitudes and longitudes provided in Table 1.

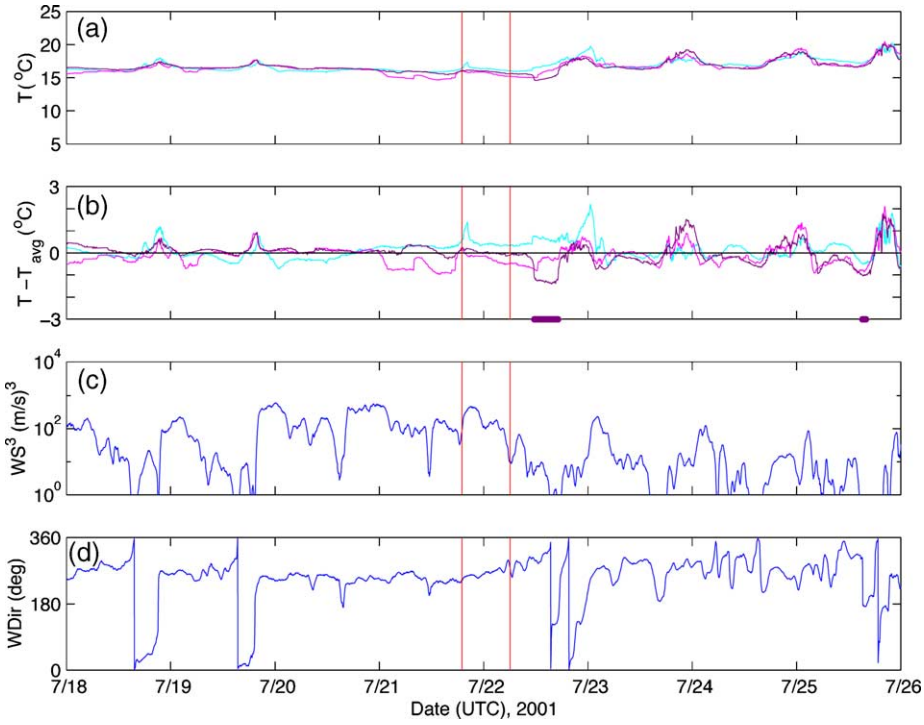

Fig. 7. Field data corresponding to July 2001 images. (a) Average water temperature measured by the Stowaway thermistors at the NASA buoys. TB1 = blue, TB2 = cyan, TB3 = magenta, TB4 = purple. Blue shades denote the two eastern buoys, while purple shades denote the two western buoys. The darker shades denote the two northern buoys, while the lighter shades denote the two southern buoys. (b) Difference from the 12-h running mean of the average temperature for all buoys. Colored dots on the x-axis indicate points more than 1 °C cooler than the 12-h running mean temperature. (c) Wind speed cubed (analog of wind power) computed from wind speed measured at TB3. (d) Wind direction (WDir) measured at TB3, in degrees clockwise from True North. Red vertical lines denote the times of MODIS images. Buoy locations shown in Fig. 4, and latitudes and longitudes provided in Table 1.

Upwellings should be evident in the field data as short-term drops in the skin temperature that dominate and overwhelm the usual diurnal heating and cooling cycle. They should also coincide with periods of strong, sustained winds. Upwellings should be evident in the thermal infrared images as cool patches near the upwind shore of the lake.

The ETM+/ASTER day/day image pair acquired June 3, 2001 (Fig. 3a,b) and MODIS images acquired June 3–4, 2001 (Fig. 3c,d) show a large partial upwelling event following elevated winds, which were predominantly from the west–southwest. The median skin temperatures of the ETM+ and ASTER images were 12.8 °C and 12.9 °C, respectively. The median skin temperatures of the June 3rd and June 4th MODIS images were 13.1 and 11.8 °C, respectively. The short interval of separation between the ETM+ (Fig. 3a) and ASTER (Fig. 3b) images allows the demonstration of the similarities between the ETM+ and ASTER images. The patterns in these images indicate that cool, metalimnetic water has upwelled on the west (upwind) side of the lake as a distinct jet. The water masked in dark purple along the western shore of the June 3, 2001 images (Fig. 3a–c) is more than 4 °C cooler than the median temperature of the water surface. This is consistent with the temperature of water brought up from below the top of the spring metalimnion, which is typically at a depth of 10–20 m (based on temperature profile data (not shown) measured at the LTP Station (Fig. 1) for June 2003). The bifurcation of the cool water jet on the east side of the lake indicates divergence of the flow as it is entrained into two separate surface gyres. The displacement of the jet front observed in the high-resolution images in Fig. 3a,b indicates a surface transport rate of this upwelled water of approximately 12 cm/s across the lake in a south-easterly direction, as determined by multiplying the displacement of the leading edge of the jet (3 pixels) by the pixel size (90 m) and dividing by the time elapsed between the two images (38 min).

The MODIS images acquired June 3, 2001 (Fig. 3c) at the same time as the ASTER image and ~11 h later on June 4, 2001 (Fig. 3d) provide further evidence of the large-scale gyral transport as the cool thermal feature is advected north–south along the eastern shore. The general patterns evident in the June 3, 2001 MODIS image correspond closely with the patterns visible in the high resolution ASTER/ETM+ images. However, the sharpness of the frontal structures and the secondary circulations, clearly evident in the high-resolution images in Fig. 3a,b, cannot be clearly resolved in the MODIS image in Fig. 3c. The larger time separation between the MODIS images allows the patterns to change significantly, through rotation, dispersion, and sinking, between successive image acquisitions. For example, dispersion and rotation signifi-

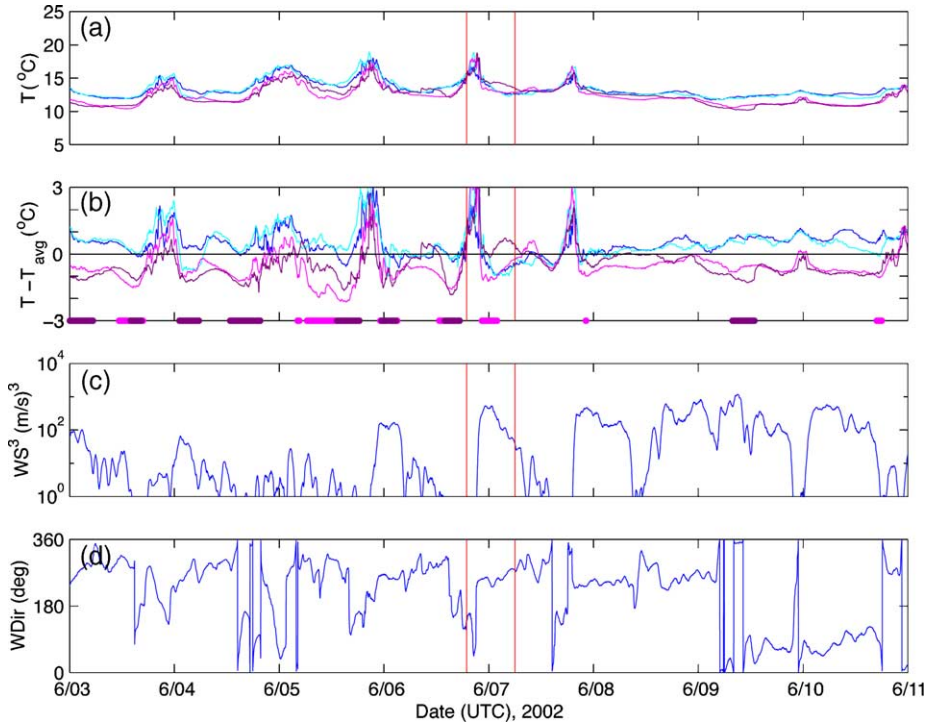

Fig. 8. Field data corresponding to June 2002 images. (a) Average water temperature measured by the Stowaway thermistors at the NASA buoys. TB1 = blue, TB2 = cyan, TB3 = magenta, TB4 = purple. Blue shades denote the two eastern buoys, while purple shades denote the two western buoys. The darker shades denote the two northern buoys, while the lighter shades denote the two southern buoys. (b) Difference from the 12-h running mean of the average temperature for all buoys. Colored dots on the *x*-axis indicate points more than 1 °C cooler than the 12-h running mean temperature. (c) Wind speed cubed (analog of wind power) computed from wind speed measured at TB3. Red vertical lines denote the times of MODIS images. Buoy locations shown in Fig. 5, and latitudes and longitudes provided in Table 1. (d) Wind direction (WDir) measured at TB3, in degrees clockwise from True North.

cantly altered the shape and horizontal extent of the upwelling jet. Furthermore, the upwelled water visible along the southern shore in the June 3, 2001 images is not apparent in the June 4, 2001 MODIS image (Fig. 3d), possibly due to sinking of this cooler, denser water.

Table 4
Acquisition data for ASTER, ETM+, and MODIS upwelling images

Event #	Instrument	Image date	Image time (UTC)	Instrument	Image date	Image time (UTC)
1	ASTER	Apr 29, 2000	19:11	MODIS	Apr 29, 2000	19:13
	ASTER	Apr 30, 2000	06:16	MODIS	Apr 30, 2000	06:17
2	ASTER	Jul 18, 2000	19:11	MODIS	Jul 18, 2000	19:12
	ASTER	Jul 19, 2000	06:16	MODIS	Jul 19, 2000	06:16
3	ETM+	Aug 19, 2000	18:29	MODIS	Aug 19, 2000	19:11
	ASTER	Aug 19, 2000	19:11	MODIS	Aug 20, 2000	06:16
4	ETM+	Jun 03, 2001	18:28	MODIS	Jun 03, 2001	19:06
	ASTER	Jun 03, 2001	19:06	MODIS	Jun 04, 2001	06:10
5	ETM+	Jul 21, 2001	18:28	MODIS	Jul 21, 2001	19:05
	ASTER	Jul 22, 2001	06:09	MODIS	Jul 22, 2001	06:09
6	ETM+	Aug 22, 2001	18:27	MODIS	Aug 22, 2001	19:04
	ASTER	Aug 22, 2001	19:04	MODIS	Aug 23, 2001	06:08
7	ASTER	Jun 06, 2002	18:58	MODIS	Jun 06, 2002	18:58
	ASTER	Jun 07, 2002	06:02	MODIS	Jun 07, 2002	06:03
8	ETM+	Jun 22, 2002	18:27	MODIS	Jun 22, 2002	18:58
	ASTER	Jun 22, 2002	18:58	MODIS	Jun 23, 2002	06:02
9	ETM+	Sep 10, 2002	18:26	MODIS	Sep 10, 2002	18:58
	ASTER	Sep 10, 2002	18:58	MODIS	Sep 11, 2002	06:02

Representative field data for this event are displayed in Fig. 6. A large wind event during June 1–3, 2001 from the southwest (Fig. 6c,d) initiated an upwelling event throughout this period. This is the predominant direction for strong winds at Lake Tahoe. The temperature records in Fig. 6a show significant cooling and disruption of the diurnal cycle. The water temperatures at TB3 and TB4 drop more than 1 °C below the 12-h running mean of the buoy temperatures (Fig. 6b). The temperatures at TB3 and TB4 vary considerably, at times rising higher than temperatures at TB1 and TB2. This can be attributed to surface circulation, internal-wave fluctuations, where the upwelled water intermittently drops below the depth of the in situ temperature sensors, and the surface skin effect, where diurnal warming of the skin masks the signal at the surface, or when the cold water jet does not pass under the buoy and is therefore not detected. This effect was also evident in measurements acquired during a full winter upwelling in Lake Tahoe in January, 2000 (Schladow et al., 2004). At the time of the ASTER/MODIS overpass on June 3rd, the coldest part of the jet reached TB2, as reflected in the field data. By the time of the MODIS overpass on June 4th, the temperatures at the buoys became more homogeneous. However, the MODIS image in Fig. 3d indicates that the streak from the cold jet was transported south and east of the buoys as the bifurcated section was transported north–south along the

eastern shore. Warming or sinking of the cool water in the central part of the jet is apparent in the June 4th MODIS image, but the jet no longer intersected the buoys. Another wind event during June 5–6, 2001 initiated another upwelling, as evidenced by the in situ temperature record. The signal is more pronounced than for the previous upwelling, possibly due to the thermocline oscillations excited by the cumulative forcing of the June 1–3, 2001 wind events. One MODIS image (not shown) was available to verify this event. Although there was some cloud contamination present, upwelling is apparent along the western shore. However, high-resolution ASTER and ETM+ imagery were not available to verify or properly characterize this event.

The ETM+/ASTER day/night image pair acquired July 21–22, 2001 (Fig. 4a,b) and MODIS images acquired July 21–22 (Fig. 4c,d) show another significant partial upwelling event. The median skin temperatures of the ETM+ and ASTER images were 16.1 and 15.8 °C, respectively. The median skin temperatures of the July 21st and July 22nd MODIS images were 16.5 and 15.8 °C, respectively. The cool water along the western shore of the July 21, 2001 images (Fig. 4a,c) is approximately 2 °C cooler than the median temperature of the water surface. This is consistent with the temperature of water brought up from below the top of the summer metalimnion, which is typically at a depth of 20–30 m (based on temperature profile data (not shown) measured at the LTP Station (Fig. 1) for July 2003). The displacement of the jet front observed in the high-resolution images in Fig. 4a,b indicates a surface transport rate of this upwelled water of approximately 17 cm/s across the lake in a south-easterly direction, again in a jet-like manner, as determined by multiplying the displacement of the leading edge of the jet (80 pixels) by the pixel size (90 m) and dividing by the time elapsed between the two images (11 h 41 min). ASTER and ETM+ images (not shown) acquired July 18–19, 2000 and August 19–20, 2000 (Table 3) show similar jet-like features to the June 3, 2001 and July 21–22, 2001 events.

These images enable the comparison of a high resolution image pair with a moderate-resolution image pair. The thermal feature evident in the ETM+ image (Fig. 4a) is not well-resolved in the corresponding MODIS image (Fig. 4c). Similarly, after advection across the lake in the form of a surface jet, this feature is clearly resolved in the ASTER image (Fig. 4b), but is not clearly resolved in the MODIS image (Fig. 4d), since the larger MODIS pixels average the cool jet with the warmer water surrounding it. Furthermore, there is evidence of a clockwise gyre in the southern section of the lake in both of the high-resolution images. This feature is obscured in the MODIS images. The southward transport of the warm feature in the northeast could be the result of downwelling in the region of the jet shown in the July 22, 2001 images.

The field data show several moderate (7–12 m/s) wind events, primarily from the west–southwest (Fig. 7c,d), in the days preceding the upwelling that was initiated on July 21, 2001 (Fig. 7a,b). There is a lag between the last wind peak and the upwelling peak. The buoy temperature signal at TB3 records the upwelling event, but by the time of the ETM+ and MODIS overpasses on July 21st, the temperatures at the buoys were fairly homogeneous. The jet evidently intersected TB3 as it moved southeast, bypassing TB4. The bulk water temperature at TB4 did not drop until after the ASTER/MODIS overpass on July 22nd, as the main upwelling front reached this buoy. A more gradual drop in temperature is evident at TB3.

The ASTER/ASTER day/night pair acquired June 6–7, 2002 (Fig. 5a,b) and corresponding MODIS images (Fig. 5c,d) show an event that was not immediately captured by the field data. The median skin temperatures of the daytime and nighttime ASTER images were 15.7 and 12.7 °C, respectively. The median skin temperatures of the June 6th and June 7th MODIS images were 16.6 and 13.0 °C, respectively. The ASTER image in Fig. 5a shows a partial upwelling event in the southern section of Lake Tahoe. This is significant, since upwelling predominantly occurs in the western section of the lake. The cool water is eventually advected north–westward (Fig. 5b,d). The ASTER and MODIS daytime images in Fig. 5a and c, respectively, show similar patterns. However, these are not well-resolved in the MODIS image, especially a warm thermal feature in the southwest section of the lake in the ASTER image. The ASTER and MODIS nighttime images in Fig. 5b and d are highly correlated, with even smaller-scale features clearly resolved in the MODIS image.

The field data show elevated winds, initially from the south (Fig. 8c,d), turning towards the west as the winds increased on June 6, 2002, indicating the possibility of an upwelling from the southwest or west, as evident in Fig. 5a,c. The thermistor temperatures (Fig. 8a,b) drop at TB3 and TB4 preceding this event, but there is no obvious feature corresponding to this event in the images in Fig. 5a,c. The water temperatures at TB1, TB2, and TB3 drop before the June 7, 2002 images were acquired, either due to advection of the cold water to the northwest or augmentation of the upwelling along the western shore, resulting from a second stronger wind event on June 7th. However, warm water advected by a counter-clockwise gyre in the north intersects all of the buoys, to varying degrees, by the time the images were acquired. A significant partial upwelling event is indicated by the field data from June 9–11, 2002 following strong winds from the southwest, which shifted to the east for a day, and then back to the west. A MODIS image (not shown) acquired June 10, 2002 (18:30 GMT) shows what appears to be a bifurcated jet, similar in appearance to the jet in Fig. 3a–c, but the cool water near the eastern shore could have been influenced by upwelling on the east side of the lake, resulting from the strong easterly winds. However, high-resolution ASTER and ETM+ data were not available to verify or properly characterize this event.

3.1. Upwelling and lake clarity

The satellite images shown indicate features than may have great bearing on ecological measurements made at Lake Tahoe and at other lakes and reservoirs. Chlorophyll, nutrient, primary productivity, and clarity measurements have been taken at the LTP and MLTP (Mid-Lake Tahoe Productivity) stations (Fig. 1) since July 1967 and December 1969, respectively (Jassby et al., 1999). The images presented above show that both of these sites are affected by partial upwelling and the subsequent transport of formerly deep water across the lake surface. Many of the measurements have undoubtedly been taken at times of upwelling. The time lag that is frequently present between the time of high wind speed and the upwelling jet (~1 day) also contributes to this likelihood, as water is rarely sampled on windy days.

Secchi depth and chlorophyll data were analyzed for 2001–2002. Averaged daily wind power (analog of upwelling) was found to be inversely correlated with Secchi depth, with correlation coefficients of 0.51 and 0.49 for 2001 and 2002, respectively. Using the *t*-distribution with 29 and 31 degrees of freedom for 2001 and 2002, respectively, correlation coefficients greater than 0.31 and 0.30 are statistically significant at the 95% confidence level. The maximum correlation occurred at a lag of one day. These correlations indicate that large winds (upwelling) generally decrease Secchi depth. This would correspond with transport of chlorophyll and inorganic particles from the metalimnion, where they are found in greater concentrations, into the surface layer. However, no strong correlation could be found with composite (depth-averaged) chlorophyll. This is probably due to the fact that there should be some lag time (>1–2 days) between nutrient influx into the epilimnion and increased productivity. Since partial upwellings occur with great regularity, sometimes daily, this could mask the effect of partial upwelling on chlorophyll, especially given the sparse nature of chlorophyll sampling.

The strong correlation between upwelling and reduced clarity is the result of a large number of upwellings that come from moderate depth, where there are greater concentrations of particles, both organic and inorganic. Although the correlation is strong, it should not be expected to be perfect. First, the Secchi depth readings are sparse, with one reading every 1–2 weeks. Second, if a partial upwelling is strong, it will bring up very clear water from below the chlorophyll and particle maxima, and the clarity should increase, as has been observed following winter upwelling. For example, clarity increased between successive Secchi depth readings on June 11, 2001 and July 25, 2001, despite the occurrence of an upwelling on July 21, 2001. The strength of this upwelling is indicated by the ASTER image in Fig. 3b. This event was followed by an increase in composite (total) chlorophyll between successive readings on July 16, 2001 and July 25, 2001. Chlorophyll profile data show that the depth of the chlorophyll maximum dropped between June 11, 2001 and July 25, 2001, with a corresponding decrease in chlorophyll between 0–20 m. Therefore, upwellings can be expected to increase the variability in clarity, with frequent moderate upwellings decreasing clarity and infrequent strong upwellings generally increasing clarity.

4. Conclusions

Thermal infrared images acquired by ASTER, Landsat ETM+, and MODIS can be used to observe partial upwelling events in lakes and can provide a measure of their spatial variability and horizontal distribution, information totally lacking from conventional measurement systems such as thermistor chains. The images have enabled the identification of partial upwellings and the horizontal transport associated with them as important and persistent features in Lake Tahoe. They are seen to occur every few days throughout the spring and summer, transporting water from 10–30 m below the surface to the surface layer. They commonly display a jet-like appearance, traveling from the upwind to the downwind side of the lake, with current speeds of 12 –17 cm/s. Partial upwellings were found to generally decrease lake clarity, although deeper upwelling events can increase clarity. Sinking zones, other convergence areas, and divergence areas can also be seen. These are important events that contribute to the patchiness and heterogeneity that characterize natural aquatic systems. The spatial variability evident in the thermal infrared satellite images illustrates the advantages of synoptic thermal infrared satellite measurements over in situ point measurements alone to detect upwelling events, since, depending on location, in situ temperature sensors, such as on the buoys, might not capture an upwelling event. Satellite imagery used in conjunction with in situ lake measurements can provide a spatial context for the in-lake data, describing the spatial extent and variability of lake processes.

The higher resolutions of the ASTER and ETM+ images show the surface transport more clearly than MODIS, but the temporal frequency of the high-resolution measurements is not sufficient to capture all of the upwelling events, which typically only last a few days. However, high-resolution thermal infrared images from ASTER and ETM+ can help interpret moderate-resolution infrared measurements from MODIS Terra/Aqua, which are available more frequently, up to four times per day. The spatial information conveyed by the synoptic satellite measurements can help improve monitoring of the clarity and general water quality of Lake Tahoe and other lakes. Furthermore, the understanding of the transport and mixing processes determined from analyzing these images can be used to better model water quality and design water protection standards and methods.

5. Future work

To better assess the effect of upwelling on lake clarity, multispectral optical sensors will be installed at TB3 in 2006 to provide continuous information on changes in water quality.

Acknowledgements

This work was supported by the NASA Earth System Science Fellowship, the National Science Foundation under grants OCE-9907557, OCE99-07110, and OCE99-06924, and grant 01-174-160-0 from the Lahontan Regional Water Quality Control Board. Part of the research was conducted at the Jet Propulsion Laboratory, Caltech. R. C. Richards and A. Abtahi assisted with data collection. R. Alley provided atmospheric corrections for the satellite images and buoy radiometer data. The Tahoe Environmental Research Center (TERC) provided chlorophyll and Secchi depth data, and the Tahoe Regional Planning Agency (TRPA) provided meteorological data. We would also like to thank our guest editor, Alan Gillespie, and the four anonymous reviewers for their constructive comments and suggestions, which helped improve this paper.

References

Abbott, M. R., Denman, K. L., Powell, T. M., Richerson, P. J., Richards, R. C., & Goldman, C. R. (1984). Mixing and the dynamics of the deep chlorophyll maximum in Lake Tahoe. *Limnology and Oceanography*, *29*(4), 862–878.

Barnes, W. L., Pagano, T. S., & Salomonson, V. V. (1998). Prelaunch characteristics of the Moderate Resolution Imaging Spectroradiometer (MODIS) on EOS–AM1. *IEEE Transactions on Geoscience and Remote Sensing*, *36*(4), 1088–1100.

Barsi, J. A., Schott, J. R., Palluconi, F. D., Heider, D. L., Hook, S. J., Markham, B. L., et al. (2003). Landsat TM and ETM+ thermal band calibration. *Canadian Journal of Remote Sensing*, *29*(2), 141–153.

Choubey, V. K. (1998). Laboratory experiment, field and remotely sensed data analysis for the assessment of suspended solids concentration and Secchi depth of the reservoir surface water. *International Journal of Remote Sensing*, *19*(17), 3349–3360.

Farrow, D. E., & Stevens, C. L. (2003). Numerical modelling of a surface-stress driven density-stratified fluid. *Journal of Engineering Mathematics*, *47*(1), 1–16.

Hook, S. J., Prata, F. J., Alley, R. E., Abtahi, A., Richards, R. C., Schladow, S. G., et al. (2003). Retrieval of lake bulk and skin temperatures using Along-Track Scanning Radiometer (ATSR-2) data: A case study using Lake Tahoe, California. *Journal of Atmospheric and Oceanic Technology*, *20*(4), 534–548.

Howarth, R. W. (1993). The role of nutrients in coastal waters. *Managing waste water in coastal urban areas, Appendix A* (pp. 137–158). Washington, D.C.: National Academy Press.

Ikeda, M., & Emery, W. J. (1984). A continental-shelf upwelling event off Vancouver Island as revealed by satellite infrared imagery. *Journal of Marine Research*, *42*(2), 303–317.

Jassby, A. D., Goldman, C. R., Reuter, J. E., & Richards, R. C. (1999). Origins and scale dependence of temporal variability in the transparency of Lake Tahoe, California–Nevada. *Limnology and Oceanography*, *44*(2), 282–294.

MacIntyre, S. (1993). Vertical mixing in a shallow, eutrophic lake: Possible consequences for the light climate of phytoplankton. *Limnology and Oceanography*, *38*(4), 798–817.

MacIntyre, S. (1998). Turbulent mixing and resource supply to phytoplankton. *Physical processes in lakes and oceans: American Geophysical Union* (pp. 561–590).

MacIntyre, S., Flynn, K. M., Jellison, R., & Romero, J. R. (1999). Boundary mixing and nutrient fluxes in Mono Lake, California. *Limnology and Oceanography*, *44*(3), 512–529.

MacIntyre, S., & Jellison, R. (2001). Nutrient fluxes from upwelling and enhanced turbulence at the top of the pycnocline in Mono Lake, California. *Hydrobiologia*, *466*(1–3), 13–29.

Mann, K. H. (2000). *Ecology of coastal waters, with implications for management* (2nd edn.). Boston: Blackwell Science.

Monismith, S. G. (1985). Wind-forced motions in stratified lakes and their effect on mixed-layer shear. *Limnology and Oceanography*, *30*(4), 771–783.

Monismith, S. G. (1986). An experimental study of the upwelling response of stratified reservoirs to surface shear stress. *Journal of Fluid Mechanics*, *171*, 407–439.

Ostrovsky, I., Yacobi, Y. Z., Walline, P., & Kalikhman, I. (1996). Seiche-induced mixing: Its impact on lake productivity. *Limnology and Oceanography*, *41*(2), 323–332.

Rogers, R. H., Shah, N. J., McKeon, J. B., & Smith, V. E. (1976). Computer mapping of water-quality in Saginaw Bay with Landsat digital data. *Photogrammetric Engineering and Remote Sensing*, *42*(6), 831.

Rueda, F. J., Schladow, S. G., & Palmarsson, S. O. (2003). Basin-scale internal wave dynamics during a winter cooling period in a large lake. *Journal of Geophysical Research*, *108*(C3), 42–41–42–16.

Salomonson, V. V., Barnes, W. L., Maymon, P. W., Montgomery, H. E., & Ostrow, H. (1989). MODIS: Advanced facility instrument for studies of the earth as a system. *IEEE Transactions on Geoscience and Remote Sensing*, *27*(2), 145–153.

Schladow, S. G., Palmarsson, S. O., Steissberg, T. E., Hook, S. J., & Prata, F. J. (2004). An extraordinary upwelling event in a deep thermally stratified lake. *Geophysical Research Letters*, *31*, L15504.

Stevens, C., & Imberger, J. (1996). The initial response of a stratified lake to a surface shear stress. *Journal of Fluid Mechanics*, *312*, 39–66.

Strub, P. T., & Powell, T. M. (1986). Wind-driven transport in stratified closed basins: Direct versus residual circulations. *Journal of Geophysical Research*, *91*, 8497–8508.

Strub, P. T., & Powell, T. M. (1987). Surface temperature and transport in Lake Tahoe: Inferences from satellite (AVHRR) imagery. *Continental Shelf Research*, *7*, 1001–1013.

Strub, P. T., Powell, T. M., & Abbott, M. R. (1984). Temperature and transport patterns in Lake Tahoe: Satellite imagery, field data and a dynamical model. *Verhandlungen Internationale Vereinigung fur Theoretische und Angewandte Limnologie*, *22*, 112–118.

Wing, S. R., Largier, J. L., Botsford, L. W., & Quinn, J. F. (1995). Settlement and transport of benthic invertebrates in an intermittent upwelling region. *Limnology and Oceanography*, *40*(2), 316–329.

Yamaguchi, Y., Kahle, A. B., Tsu, H., Kawakami, T., & Pniel, M. (1998). Overview of Advanced Spaceborne Thermal Emission and Reflection Radiometer (ASTER). *IEEE Transactions on Geoscience and Remote Sensing*, *36*(4), 1062–1071.